

Leandro G. Jeifetz, Pablo Daniel Giunta*, Fernando J. Mariño, Norma E. Amadeo, and Miguel Á. Laborde

Simulation of CO Preferential Oxidation (COPrOx) Monolithic Reactors

Abstract: In this work, a COPrOx monolithic reactor with a CuO/CeO₂/Al₂O₃ catalytic washcoat was modelled to purify a H₂ stream for a 2 kW PEM fuel cell. Preliminary simulations included isothermal monoliths operating between 423 and 463 K, and the optimization of linear axial temperature profiles. For a fixed total system size and a desired CO outlet molar fraction lower than 20 ppm, an isothermal temperature profile maximized the global selectivity towards CO oxidation. Then, different schemes of adiabatic monoliths with interstage cooling were modelled and evaluated. It was found that wide operating temperature ranges lower the necessary number of stages, but decrease the global selectivity and rise system sensitivity to inlet temperatures. A 1D heterogeneous model was used to simulate the monoliths.

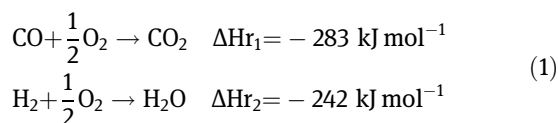
Keywords: monolithic reactor, modelling, COPrOx, PEM fuel cell, heat exchange

*Corresponding author: Pablo Daniel Giunta, Department of Chemical Engineering, Laboratorio de Procesos Catalíticos, DIQ-FI, Universidad de Buenos Aires, Pabellón de Industrias, Ciudad Universitaria, Buenos Aires 1428, Argentina, E-mail: pgiunta@fi.uba.ar
Leandro G. Jeifetz: E-mail: lejeifetz@gmail.com, Fernando J. Mariño: E-mail: fernando@di.fcen.uba.ar, Norma E. Amadeo: E-mail: norma@di.fcen.uba.ar, Miguel Á. Laborde: E-mail: miguel@di.fcen.uba.ar, Department of Chemical Engineering, Laboratorio de Procesos Catalíticos, DIQ-FI, Universidad de Buenos Aires, Pabellón de Industrias, Ciudad Universitaria, Buenos Aires 1428, Argentina

1 Introduction

Fuel cell technology is a very effective method to produce electricity. Among the different types of fuel cells, the *proton exchange membrane fuel cell* (PEMFC) is the most adequate for mobile applications due to its high power density, low weight and relatively low operation temperature. A disadvantage of these fuel cells is their high sensitivity to the presence of low amounts of CO in the feed gas; a CO concentration of 50 ppm is enough to poison the anode. When H₂ is produced by reforming or partial oxidation of alcohols or hydrocarbons, the

formation of carbon oxides (CO₂ and CO, the latter in the range of 8–12%) is unavoidable. In order to reduce the CO concentration in the H₂ stream, a water gas shift (WGS) reactor is used. Nevertheless, the WGS product gas still contains about 1% CO due to the thermodynamic limitations [1]. Different techniques for further purification are proposed, such as pressure swing absorption, H₂ separation by Pd membranes, CO methanation and CO Preferential Oxidation (COPrOx). The last one is a good alternative because of its simplicity and cost-effectiveness. An air stream is added to the feed gas and, via a suitable catalyst, CO is oxidized to CO₂. Since there is a high amount of H₂ in the stream, the catalyst must be very selective towards CO oxidation. The following reactions occur in the gas phase:



Noble metals, particularly Pt [2, 3], Au [4] and Ru [5], are used as catalysts. Moreno et al. [6], Sedmak et al. [7] and Lee and Kim [8] have demonstrated that less expensive catalysts, such as Cu–Ce catalysts, are also very active and selective for this reaction.

In a previous work, the performance of a COPrOx fixed-bed reactor was analyzed by our group [9]. In particular, the effect of different heat transfer schemes was analyzed. Moreover, monolithic reactors have certain characteristics that make them attractive for the CO preferential oxidation. A monolithic reactor is a continuous structure of parallel narrow channels where each channel has a width of about a millimetre. The walls of monolithic reactors are not good supports for active species. Therefore, a porous layer must be deposited on the walls of the channels: generally an inorganic oxide of large surface area (e.g. γ -Al₂O₃) adheres to the monolith and the active species (metals or metal oxides) are deposited on it. Monolithic reactors have the following advantages compared to fixed bed reactors: lower pressure drop, higher effectiveness factors, lower overall mass transfer resistance and easier cleaning. Their main disadvantages are: lower heat transfer coefficients, the

impossibility to compensate flow maldistributions produced at the reactor inlet and a lower catalyst load per reactor volume [10–14]. Although monolithic reactors have been extensively studied and used for the control of automobiles exhaust gases emissions, there are many emerging applications: catalytic combustion, hydrogenation reactions, oxidation of organic and inorganic compounds in aqueous solution and biochemical processes. In general, the motivations are the low pressure drop and the reduction of the diffusional resistances. One of the biggest challenges is to ensure good flow distribution in all the monolithic channels.

Among the reported antecedents of the application of monolithic reactors for COPrOx reaction, cordierite prevails as the support. Korotkikh and Farrauto [15] used a 400-cell per square inch (cpsi) monolith to study the behaviour of a Pt/ γ -Al₂O₃ commercial catalyst. Gómez et al. [16] prepared, evaluated and characterized Co/ZrO₂ catalysts; Roberts et al. [17] tried Pt/Al₂O₃ catalysts promoted with Fe and Zhou [18] tested different noble metal catalysts on Al₂O₃: in the last case, authors chose a Pt/Al₂O₃ catalyst to develop a set of four monoliths with cooling and oxygen supply between them, for a 5 kW system. The scheme of ceramic monoliths with intermediate cooling stages was also suggested by Heck et al. [13]. Ahluwalia et al. [19] developed a system of three 600 cpsi cordierite monoliths in series with intermediate cooling stages and air feed, using a commercial catalyst.

The application of metal monoliths for COPrOx was studied by Zeng and Liu [20] motivated by their higher thermal conductivity compared to ceramic monoliths. They worked with CuO/CeO₂ catalysts promoted with Nd and Zr on FeCrAl 400 cpsi monoliths. Among modelling antecedents, Bissett and Oh [21] simulated a 600 cpsi monolithic reactor for a 50 kW system, with a Pt catalyst. First, authors carried out an isothermal modelling of the monolith, and then they simulated schemes of adiabatic reactors with two, three and four cooling interstages. Depcik and Srinivasan [22] performed a parameter study of a 1D + 1D monolith catalyst for the CO conversion during a light-off experiment using an uniform washcoat and a layered washcoat with dissimilar catalyst materials, showing the influence of the conversion upon the order of the layers. Tronconi et al. [23] performed a 1D simulation of 200–400 cpsi copper honeycomb monoliths washcoated with Pd/ γ -Al₂O₃ for the CO oxidation reaction, showing results in good agreement with experimental data. Arzamendi et al. [24] studied the behaviour of the COPrOx with CuCe catalysts in microchannels and microslits, showing a reasonable agreement between experimental data and model results.

In this work, a monolithic reactor for COPrOx stage is modelled. This reactor is aimed to purify an H₂ stream feeding a 2 kW PEMFC, reducing CO concentration to less than 20 ppm. In agreement with the antecedents, extruded cordierite monoliths of square channels are used in the simulation. A CuO/CeO₂/Al₂O₃ catalytic washcoat is adhered to the cordierite support. The main objective of the manuscript is to estimate good operation temperatures of a series of adiabatic monoliths with interstage cooling to use the results as guidelines for future simulations, rather than calculate the optimal reactor design and operating conditions.

A water–alcohol mixture (the reformer feed) could be conveniently split as coolant stream in order to pre-heat itself before entering the reforming unit. This alternative contributes to the energy integration of the overall system [9].

First, an isothermal monolith is modelled to assess the effect of the temperature on the required mass of catalyst (and therefore on the reactor volume) and on the global selectivity. Then, linear axial temperature profiles are evaluated to maximize the global selectivity (given this restriction of linear profiles) and to orientate the desirable temperature profile in a series of adiabatic monoliths (cordierite monoliths are virtually adiabatic [11]). Last, schemes of adiabatic monoliths with interstage cooling operating in different temperature ranges are compared regarding their global selectivity, the number of stages and the sensitivity to inlet temperatures. Future work will include experimental results for model validation.

2 Methodology

2.1 Geometrical parameters

A representative unit cell is used to geometrically describe the monolithic reactor. The cell includes a square channel and the cordierite support around it. A scheme of the cross section and the geometrical parameters are presented in Figure 1 [25, 26].

The cell side length is called m and the cordierite support thickness between two consecutive channels is β . As the catalytic washcoat tends to accumulate in the corners of the channels, its thickness is defined by $\delta/2$ and Rc : the first parameter is the thickness far from the channel corner, while the second one is the radius in the corner. From these parameters, unit cell cross section fractions occupied by the cordierite support, the catalytic

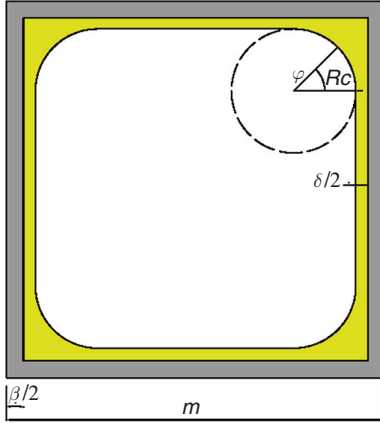


Figure 1 Square channel transversal section in a monolithic reactor. Geometrical parameters

washcoat and the flowing gas (α , ξ and ε , respectively) are calculated according to eqs (2)–(4).

$$\alpha = \frac{4 \left(\frac{\beta}{2}\right) \left(m - \frac{\beta}{2}\right)}{m^2} \quad (2)$$

$$\xi = \frac{4 \left(\frac{\delta}{2}\right) \left(m - \beta - \frac{\delta}{2}\right) + 4Rc^2 - \pi Rc^2}{m^2} \quad (3)$$

$$\varepsilon = 1 - \alpha - \xi \quad (4)$$

The channel perimeter (per_{ch}), the cross section area for open gas flow (a_{ch}), and the hydraulic diameter (d_{h}) are calculated according to eqs (5)–(7).

$$a_{\text{ch}} = \varepsilon m^2 \quad (5)$$

$$\text{per}_{\text{ch}} = 4(m - \beta - \delta - 2Rc) + 2\pi Rc \quad (6)$$

$$d_{\text{h}} = \frac{4a_{\text{ch}}}{\text{per}_{\text{ch}}} \quad (7)$$

Given the monolith internal diameter (d_i), the number of channels (n_{ch}) is calculated according to eq. (8). For a determined monolith length (L), the total catalyst mass (tcm) is calculated from eq. (9).

$$n_{\text{ch}} = \frac{\pi d_i^2}{4m^2} \quad (8)$$

$$\text{tcm} = \frac{\pi d_i^2}{4} L \rho_{\text{WP}} \xi \quad (9)$$

2.2 Mass and energy balances

The model employed in this work, which is described in this section, is taken from Tronconi et al. [23].

Isothermal monoliths are initially modelled, then linear axial temperature profiles along the monoliths are considered and last, adiabatic monoliths are simulated. Therefore, in all the cases radial isothermicity is assumed. Flow distribution among the different channels is considered to be homogeneous. These hypotheses allow to assume a single channel as representative of the others [27].

This channel is represented with a steady-state, 1D heterogeneous model, in agreement with other authors [21, 23]. Pressure drop and axial mass and heat dispersion in the gas phase are considered negligible, according to the works referenced. Effectiveness factors are approximated to unity (see Appendix C) and the gas phase is considered an ideal gas. Mass and energy balances in the channel are presented in eqs (10)–(13).

Species mass balances in the gas phase:

$$\frac{dF_i^G}{dz} = -km_i(y_i^G - y_i^S)\text{per}_{\text{ch}} \quad (10)$$

Species mass balances in the washcoat surface:

$$km_i(y_i^G - y_i^S)\text{per}_{\text{ch}} = -\frac{r_i^S \rho_{\text{WP}} \xi a_{\text{ch}}}{\varepsilon} \quad (11)$$

Energy balance in the gas phase:

$$\frac{dT^G}{dz} = -\frac{h_{\text{GS}}(T^G - T^S)\text{per}_{\text{ch}}}{\sum_i F_i^G C_{p_i}^G \varepsilon} \quad (12)$$

Energy balance in the solid phase (cordierite support and catalytic washcoat):

$$\frac{d^2 T^S}{dz^2} = \frac{4h_{\text{GS}}\varepsilon}{\kappa_{\text{ax}}^{\text{ef}} d_{\text{h}}} (T^S - T^G) + \frac{\rho_{\text{WP}} \xi}{\kappa_{\text{ax}}^{\text{ef}}} \sum_m \Delta H_{r_m} r_m \quad (13)$$

The boundary conditions are:

$$\text{In } z = 0: F_i^G = F_i^{G,e}, T^G = T^{G,e}, \frac{dT^S}{dz} = 0$$

$$\text{In } z = L: \frac{dT^S}{dz} = 0$$

It should be noted that the energy balances are only taken into consideration when monoliths are modelled as adiabatic. When axial isothermicity or arbitrary axial temperature profiles are assumed, only the mass balances are considered.

The kinetic expressions and the washcoat density value (ρ_{WG}) are presented in Appendix A. The mass and heat transfer coefficients (km_i and h_{GS}) and the solid phase effective thermal conductivity ($\kappa_{\text{ax}}^{\text{ef}}$) calculations are detailed in Appendix B.

Oxygen stoichiometric excess (λ) is expressed according to eq. (14). The global selectivity (S) and the reactants conversion (x_i) are calculated from eqs (15) and (16).

$$\lambda = \frac{2F_{O_2}^{G,e}}{F_{CO}^{G,e}} \quad (14)$$

$$S = \frac{F_{CO}^{G,e} - F_{CO}^{G,f}}{2(F_{O_2}^{G,e} - F_{O_2}^{G,f})} \quad (15)$$

$$x_i = \frac{F_i^{G,e} - F_i^{G,f}}{F_i^{G,e}} \quad i = CO, H_2 \quad (16)$$

To evaluate the difference between the CO outlet molar fraction and 19 ppm (19 ppm is taken as a reference value under 20 ppm), g is defined as shown in eq. (17). The restriction $g = 0$ is adopted for all the simulations.

$$g = y_{CO}^f - 19 \text{ ppm} \quad (17)$$

2.3 System resolution

The boundary value problem is solved by a finite difference code. As this code handles systems of first-order ordinary differential equations (ODEs), the second-order equation (13) must be written as two first-order ODEs. When energy balances are not taken into consideration, the initial value problem is solved using an explicit Runge–Kutta 4 method.

3 Results and discussion

3.1 Base geometrical parameters and operative conditions

The geometrical parameters adopted for all the simulations are listed in Table 1.

In Table 1, m and β values belong to a 600 cpsi commercial cordierite monolith. $\delta/2$ is adopted in agreement with Valentini et al. [28] and d_i corresponds to the internal diameter of a tube (DN 3 in, Sch 40) where the monolith could be inserted. The other parameters in Table 1 are calculated from eqs (2) to (9).

The operation conditions used in all the simulations are listed in Table 2.

The total molar flow contains 0.025 mol/s of H_2 , which equals 2.015 Nm³/h. If the H_2 consumption at COPrOx stage is low, this H_2 flow is enough to feed a 2 kW PEMFC (estimating 1 Nm³/h of H_2 per kW [29]). The inlet pressure and the composition ($\lambda = 2$) are those adopted by Giunta et al. [9].

Table 1 Base geometrical parameters

m	$1.04 \times 10^{-3} \text{ m}$
β	$88.9 \times 10^{-6} \text{ m}$
$\delta/2$	$30 \times 10^{-6} \text{ m}$
Rc	$100 \times 10^{-6} \text{ m}$
d_i	$77.9 \times 10^{-3} \text{ m}$
α	0.1637
ξ	0.1101
ε	0.7262
a_{ch}	$0.7855 \times 10^{-6} \text{ m}^2$
per_{ch}	$3.393 \times 10^{-3} \text{ m}$
d_h	$0.9261 \times 10^{-3} \text{ m}$
n_{ch}	4410
tcm/L	0.606 kg/m

Table 2 Base operative conditions

$F_{total}^{G,e}$	0.05 mol/s
$F_{CO}^{G,e}$	$1.134 \cdot 10^{-5} \text{ mol/s}$
$y_{H_2}^e$	0.5
y_{CO}^e	0.01
$y_{CO_2}^e$	0.18
$y_{O_2}^e$	0.01
$y_{H_2O}^e$	0.3
p^e	303975 Pa

3.2 Isothermal monoliths

Adopting the base parameters and conditions, isothermal reactors are simulated for different operation temperatures between 423 and 463 K. For each temperature, the reactor length L (and consequently the tcm) is fixed to achieve the desired outlet CO molar fraction ($g = 0$). This enables to compare the global selectivity at different temperatures for identical CO conversion. In every case, the catalyst and the reactor are selective enough to avoid complete O_2 conversion by H_2 oxidation. When temperature rises, the catalytic activity increases and therefore L and tcm reduce, as illustrated in Figure 2. On the other hand, since the apparent activation energy for H_2 oxidation is higher than that for CO oxidation, temperature rise decreases selectivity, hence elevating H_2 conversion (Figure 3), which in turn produces an extra heat evolution, generating a vicious circle. Therefore, a compromise between selectivity and the total catalyst mass arises from an operation temperature increase. In order to study the effect of λ , simulations are carried out for $\lambda = 4$ and $\lambda = 1.5$. The results are also shown in Figures 2 and 3.

It can be noticed that at the highest temperatures analysed, the tcm decrease becomes less pronounced,

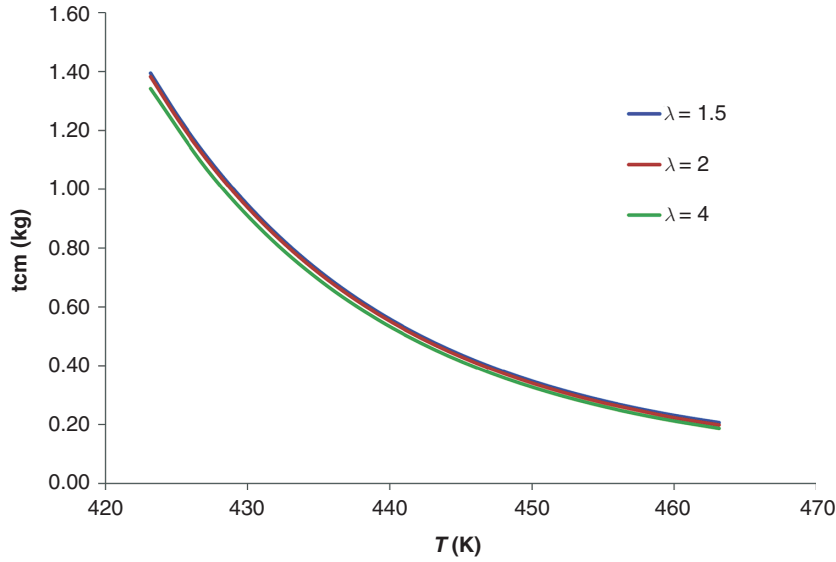


Figure 2 Total catalyst mass vs. temperature, for different λ values

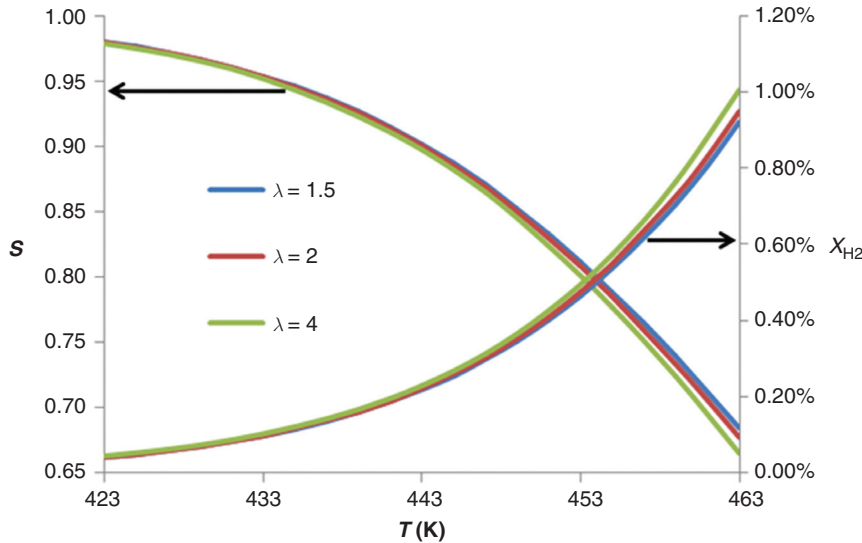


Figure 3 Selectivity vs. temperature for different λ values and H_2 conversion vs. temperature for different λ values

while the selectivity loss turns more important. At low temperatures, a moderate increase in selectivity becomes increasingly expensive in terms of the catalyst mass. This shows the convenience of operating at intermediate temperatures in the examined range.

In accordance with other authors [30], high λ values increase the catalytic activity and decrease the catalyst mass, while they lower the selectivity. However, the effect is evidently weak. In all the following simulations, $\lambda = 2$ is used.

Finally, these isothermal reactor results show that the relative difference between y_i^G and y_i^S is lower than 1.2% for every species. This verifies one of the

mentioned advantages of monoliths, i.e. the resistance to mass transfer within the washcoat is very low and the operation takes place under a kinetic regime. Even if the resistance to mass transfer at the gas side is higher compared to packed-bed reactors, as stated by Bissett and Oh [21] and observed in this study, these effects can be safely disregarded.

3.3 Linear T vs. z profiles optimization

As stated formerly, the objective of looking for a convenient temperature profile in the reactor is to orientate the

search of a good temperature profile in a series of adiabatic monoliths. In this sense, we shall use the term *optimal* loosely, meaning that we are looking for the best profile given the restriction of a linear temperature profile and fixed CO outlet composition with the aim of maximizing the global selectivity.

For a given length and adopting base parameters and conditions, the isothermal reactor temperature necessary to achieve $g = 0$ can be calculated. If the temperature in the entire reactor is lower than this value, the desired CO conversion will not be achieved. On the other hand, if temperature in the entire reactor is higher than the isothermal required temperature, the required CO conversion can be achieved but the selectivity will be lower. An optimal T vs. z profile must maximize the selectivity while achieving $g = 0$.

A very simple approach is to look for linear T vs. z profiles, as shown in eq. (18). Although this kind of temperature profile is unlikely in a reactor governed by energy balances, the results are relevant as they clearly show the trend that optimal temperature profiles should follow.

$$T = T^e + bz \quad (18)$$

According to the results presented in the former section, an isothermal reactor of $L = 0.75$ m (which implies $t_{cm} = 0.4546$ kg) should operate at 443.7 K to reach $g = 0$, achieving a selectivity value of $S = 0.8977$. As CO conversion strongly depends on the temperature profile, for every proposed T^e , there is only one b value that achieves $g_{(T^e,b)} = 0$. This b value is found by an iterative Newton–Raphson method, as it is presented in eq. (19).

$$b_{n+1} = b_n - \frac{g(b_n)}{\frac{dg}{db}(b_n)} \quad (19)$$

In each iteration step, the derivate value in eq. (19) is numerically approximated perturbing b_n value. Every evaluation of $g_{(T^e,b)}$ implies to solve the ODEs system, which does not include energy balances.

For every pair (T^e, b) for which $g_{(T^e,b)} = 0$, the selectivity is calculated. T vs. z profiles and the corresponding selectivity values are presented in Figure 4.

It can be noticed that, among all linear profiles, the best selectivity is achieved when the reactor operation is isothermal. It should also be pointed out that almost isothermal temperature profiles lead to selectivity values that are close to the maximum.

3.4 Adiabatic monoliths with interstage cooling

In accordance to the previously mentioned antecedents, a series of adiabatic monoliths with interstage cooling is one of the most common heat transfer schemes proposed for the COPrOx stage. As the number of cooling stages increases, the scheme approximates to an isothermal behaviour which, in accordance to the former results, improves the global selectivity. However, this requires more equipment and multiplies the number of variables to control, which increases the system complexity.

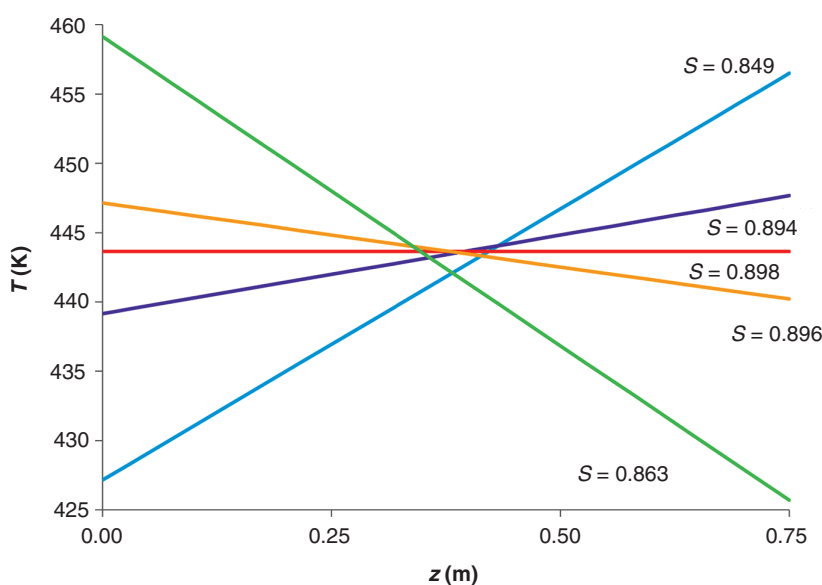


Figure 4 Temperature profiles along the reactor. Selectivity values achieved

3.4.1 Temperature ranges and selectivity

The same parameters and conditions of Section 3.3 are used. In this case, $L = 0.75$ m is the total length, which is the sum of all the monolith lengths (cooling stages are not taken into account). As an isothermal reactor should operate at 443.7 K, five operating ranges around 443 K are proposed. The first is a 20 K wide range referred to as $\Delta 20$, where T^S increases in every stage between 433 and 453 K. Then, $\Delta T_{ad}^S = T^{S,f} - T^{S,e} = 20$ K. The following ranges get wider in 10 K ($\Delta 30$, $\Delta 40$, $\Delta 50$ and $\Delta 60$): in the last one, for example, T^S increases between 413 and 473 K. Restrictions are imposed on T^S rather than on T^G , as it is T^S the temperature that determines the reaction rates. Nevertheless, both temperature profiles are practically coincident ($T^S = T^G$) because of the elevated heat transference between the gas phase and the solid phase.

In order to operate the schemes in the desired temperature ranges, the gas phase inlet temperatures to the consecutive stages ($T_k^{G,e}$) are adopted as independent variables, while the lengths of each stage (L_k) are adopted as dependent variables. For instance, in the first monolith of the $\Delta 20$ scheme, $T_1^{G,e} = 433$ K and $T_1^{S,f} = 433$ K + 20 K = 453 K: this condition is achieved when the length of the first monolith is L_1 . In the second monolith $T_2^{G,e} = 433$ K, and the same procedure is used to determine L_2 . However, for the last reactor in every scheme (NR), the length is already determined by eq. (20).

$$L_{NR} = 0,75 \text{ m} - \sum_{k=1}^{NR-1} L_k \quad (20)$$

In addition, this reactor must achieve the desired CO conversion. Consequently, $T_{NR}^{G,e}$ is not an independent variable: it arises from the conditions imposed by eq. (20) and $g = 0$.

Temperature profiles achieved for the five different schemes are presented in Figure 5. The corresponding number of stages and the global selectivity value for each temperature range are presented in Table 3.

It can be noticed that as the operation temperature range widens, the number of required stages decreases. This strongly reduces the number of necessary reactors and heat exchange equipments. The global selectivity generally decreases (except when $\Delta 50$ and $\Delta 60$ schemes are compared), though the effect is not pronounced. As the temperature range width decreases, the selectivity tends to the corresponding value of the isothermal reactor. On the whole, taking only the global selectivity and the number of stages into account, it would seem that wide temperature ranges represent a better option.

However, these schemes are more sensitive to the inlet temperatures ($T_k^{G,e}$), as it will be shown in Section 3.4.2.

Figure 5 also shows that within each scheme, the reactor lengths increase from one stage to the following (except for L_{NR} as it is fixed by eq. (20)). This result can be explained by the fact that the reaction rates decrease, reducing heat generation as the reactants are consumed.

3.4.2 Sensitivity to $T_k^{G,e}$

Adopting the same dimensions and L_k values of the previous simulations, the inlet temperatures ($T_k^{G,e}$) are slightly changed from the original values to study the effect on the temperature profiles and selectivity at the new steady state attained. This analysis is justified if we want to analyse the effect of these changes on a reactor already constructed.

Only the results for schemes $\Delta 30$ and $\Delta 50$ are presented. In scheme $\Delta 30$, which includes four reaction stages, three cases are considered: case 1 is the original one; in case 2, the inlet temperatures of the first three reactors are raised in 1 K (this value is employed for each temperature change); in case 3, the inlet temperatures of the first two reactors are lowered in 1 K. In every case, $T_{NR}^{G,e}$ is adjusted to achieve the desired CO conversion ($g = 0$). Scheme $\Delta 50$ includes three reaction stages, in which similar changes are made. The inlet temperatures and the global selectivity values for each case in both schemes are presented in Table 4. Corresponding temperature profiles are shown in Figure 6.

When schemes $\Delta 30$ and $\Delta 50$ are compared, it can be noticed that the latter is more sensitive to the 1 K change in the inlet temperatures. Although they are not presented here, parallel studies on schemes $\Delta 20$, $\Delta 40$ and $\Delta 60$ verify that the sensitivity increases when the temperature range widens.

A comparison between cases 1 and 2 within each scheme shows that when the inlet temperature of the first reactors is raised, ΔT_{ad}^S and the reactants conversion in each of them increase. Therefore, ΔT_{ad}^S in the following reactors decreases, as lower amounts of reactants are fed. Comparing cases 1 and 3, it can be noticed that reducing the inlet temperatures in the first reactors decreases ΔT_{ad}^S and the reactants conversion in them. Consequently, a higher amount of reactants are fed to the downstream reactors, where ΔT_{ad}^S are more pronounced, especially considering that they are larger. Table 4 shows that this kind of variation is particularly prejudicial to the global selectivity.

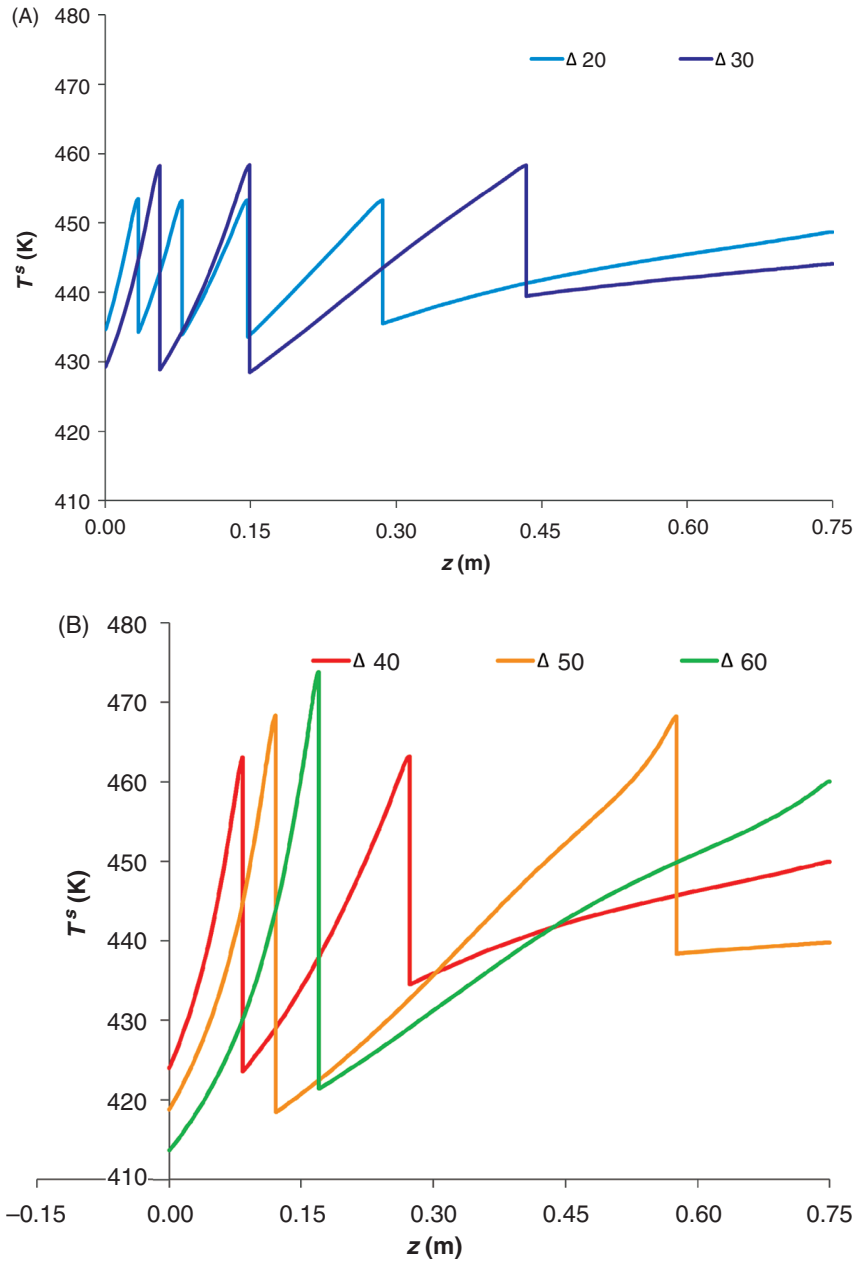


Figure 5 Temperature of the solid along the reactor: (A) $\Delta 20$ and $\Delta 30$; (B) $\Delta 40$, $\Delta 50$ and $\Delta 60$

Table 3 Number of stages and global selectivity for each scheme

Scheme	Stages	S
$\Delta 20$	5	0.888
$\Delta 30$	4	0.873
$\Delta 40$	3	0.870
$\Delta 50$	3	0.811
$\Delta 60$	2	0.830

Table 4 Inlet temperature to each stage and global selectivity for the different cases and schemes

	$\Delta 30$			$\Delta 50$		
	Case 1	Case 2	Case 3	Case 1	Case 2	Case 3
$T_1^{G,e}$	428.1	429.2	427.1	418.1	419.1	417.1
$T_2^{G,e}$	428.1	429.2	427.1	418.1	419.1	416.1
$T_3^{G,e}$	428.1	429.2	428.2	438.3	446.0	430.7
$T_4^{G,e}$	439.4	439.1	437.8	–	–	–
S	0.873	0.875	0.854	0.811	0.848	0.698

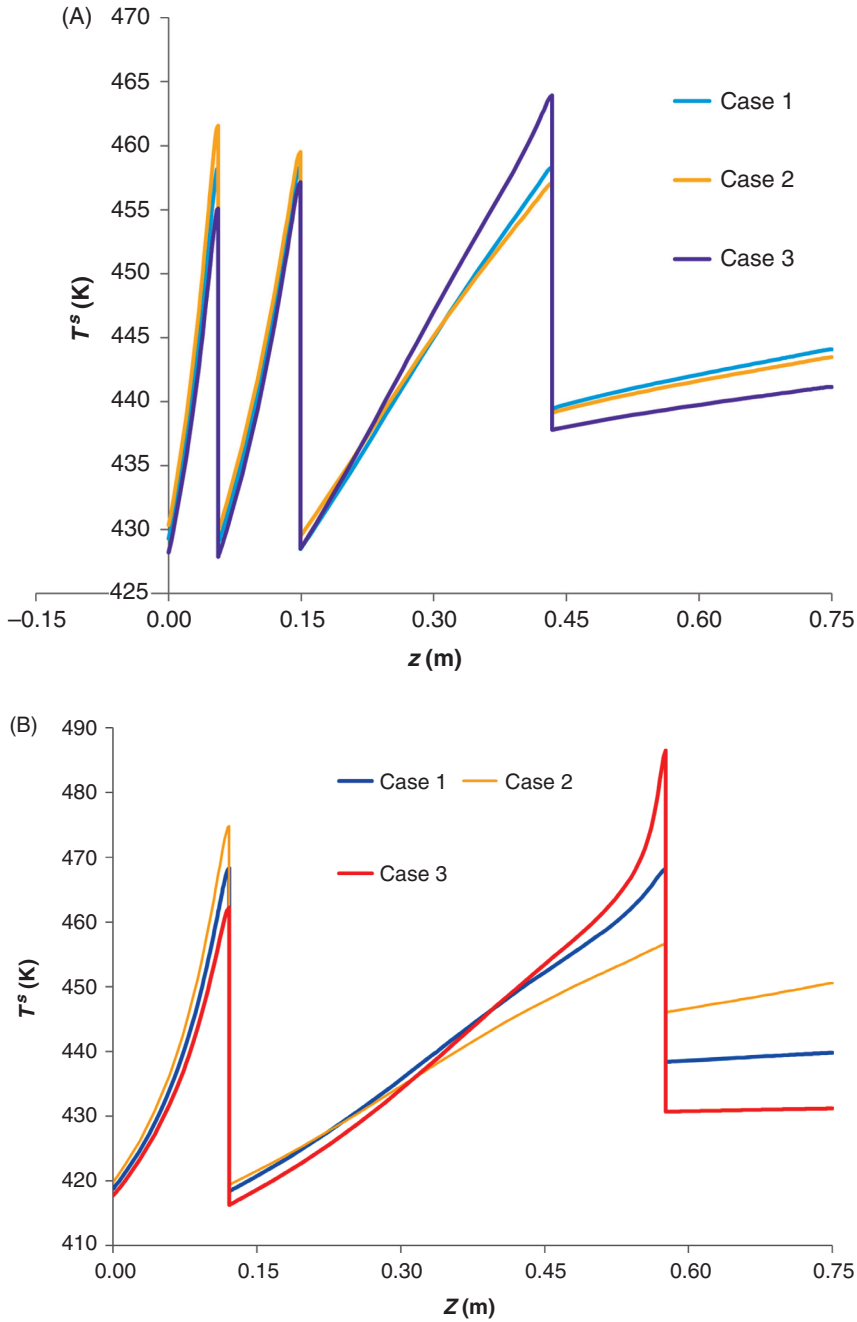


Figure 6 Modified temperature profile in the solid along the reactor: (A) $\Delta 30$; (B) $\Delta 50$

4 Conclusions

Results showed the compromise that the operation temperature generates between the global selectivity and the tcm: when temperature raises, the catalytic activity increases, but H_2 oxidation is enhanced. Intermediate temperatures are the most convenient. The linear temperature profiles show that fixing L and CO level requirement, an isothermal profile maximizes the selectivity.

As for the series of adiabatic reactors, as the temperature ranges widen, the number of stages decreases. Although selectivity only falls slightly, this renders the system highly sensitive to $T^{G,e}$: the reduction in the inlet temperatures of the first reactor produces a considerable global selectivity loss.

Acknowledgements: To ANPCYT, CONICET and University of Buenos Aires for the financial support.

Appendices

Appendix A: COPrOx kinetics and catalyst properties

The kinetic expressions were obtained by Moreno et al. [31] for a CuO (5%)/CeO₂ (30%)/Al₂O₃ catalyst.

$$-r_{\text{CO}} = \frac{k_3 K_{5,6,7} K_1 P_{\text{CO}} P_{\text{O}_2}^{1/2}}{\text{DEN}} \quad (21)$$

$$-r_{\text{H}_2} = \frac{k_{11} K_8 K_9 K_{10} K_{5,6} P_{\text{O}_2} P_{\text{H}_2}}{(\text{DEN})^2} \quad (22)$$

$$\text{DEN} = 1 + K_2 P_{\text{CO}} + K_{12} P_{\text{H}_2\text{O}} + K_8 P_{\text{H}_2} + K_{5,6,7} P_{\text{O}_2}^{1/2} (1 + K_1 P_{\text{CO}} + K_4 P_{\text{CO}_2} + K_{13} P_{\text{H}_2\text{O}}) + K_8^{1/2} K_9^{1/2} P_{\text{H}_2}^{1/2} (1 + K_{10} P_{\text{O}_2} K_{5,6})$$

According to the reactions stoichiometry, $r_{\text{CO}_2} = -r_{\text{CO}}$, $r_{\text{H}_2\text{O}} = -r_{\text{H}_2}$ and $r_{\text{O}_2} = 1/2 r_{\text{CO}} + 1/2 r_{\text{H}_2}$.

The kinetic and adsorption constants present an Arrhenius dependence on temperature, as shown in eq. (23). The corresponding values are presented in Table 5.

$$k_i = k_i^0 e^{-\frac{E_{a_i}}{RT}} \quad (23)$$

$$K_i = K_i^0 e^{-\frac{\Delta H_i^{\text{ads}}}{RT}}$$

For the same catalyst, the pore volume ($V_g = 0.44 \times 10^{-3} \text{ m}^3/\text{kg}$) was measured by Semeniuk et al. [32]. The catalytic solid density ($\rho_w = 2340 \text{ kg}/\text{m}^3$) was adopted from Elnashaie and Elshishini [33]. Then, the washcoat density was calculated as $\rho_{\text{WP}} = \rho_w / (1 + \rho_w V_g) = 1,150 \text{ kg}/\text{m}^3$.

Appendix B: transport properties

The heat and mass transfer coefficients are calculated from eqs (24) and (25), taken from Groppi and Tronconi [12].

$$\text{Nu}_{\text{GS}} = 2.977 + 6.874 \left(\frac{1,000}{\text{Gr}_t} \right)^{-0.488} \exp\left(-\frac{57.2}{\text{Gr}_t} \right) \quad (24)$$

Table 5 Kinetic and adsorption parameters for P_i in Pa, T in K and r_i in mol/g.s.

	K_1	K_2	K_3	K_4	$K_{5,6,7}$	$K_{5,6,10}$	K_8	K_9	K_{11}	K_{13}
K^0	9.77×10^{-13}	2.66×10^{-4}	1.78×10^3	1.88×10^{-10}	3.56×10^{-11}	8.19×10^{-14}	1.16×10^{-9}	3.11×10^{-9}	5.06×10^2	9.57×10^{-12}
E_a/R			5,809						5,681	
$\Delta H^{\text{ads}}/R$	-1,951	-3,605		-5,291	-12,106	-10,244	-1,081	-5,315		-7,199

Table 6 Dimensionless numbers for eqs (24) and (25)

Heat transfer		Mass transfer	
$\text{Nu}_{\text{GS}} = \frac{h_{\text{GS}} d_h}{\kappa^G}$	(26)	$\text{Sh}_i = \frac{km c_i d_h}{D_i}$	(27)
		$km_i = km c_i \left(\frac{P}{RT^G} \right)$	(28)
$\text{Gr}_t = \frac{\text{Re}_G \text{Pr}_G d_h}{z}$	(29)	$\text{Gr}_{m,i} = \frac{\text{Re}_G \text{Sc}_i d_h}{z}$	(30)
$\text{Pr}_G = \frac{\mu^G C_p^G}{\kappa^G}$	(31)	$\text{Sc}_i = \frac{\mu^G}{\rho^G D_i}$	(32)
$\text{Re}_G = \frac{\sum_i F_i^G M_i d_h}{a_{\text{ch}} \mu^G}$	(33)		

$$\text{Sh}_i = 2.977 + 6.874 \left(\frac{1,000}{\text{Gr}_{m,i}} \right)^{-0.488} \exp\left(-\frac{57.2}{\text{Gr}_{m,i}} \right) \quad (25)$$

The transport dimensionless numbers are presented in Table 6.

For each species, the diffusivity coefficient is calculated in a stagnant mixture of the other species from eq. (34), according to Wilke [33].

$$\frac{1}{D_i} = \frac{1}{1 - y_i} \sum_{j \neq i} \frac{y_j}{D_{ij}} \quad (34)$$

The solid phase effective thermal conductivity is calculated from eq. (35), according to Groppi and Tronconi [26].

$$\kappa_{\text{ax}}^{\text{ef}} = \kappa^S \alpha + \kappa^{\text{WP}} \xi \quad (35)$$

$\kappa^S = 1.3 \text{ W}/\text{m.K}$ is the cordierite thermal conductivity, and κ^{WP} is the washcoat thermal conductivity, calculated according to Poulier et al. [34].

Appendix C: effectiveness factors

The methodology to calculate the effectiveness factors of both reactions is taken from the works of Gonzo [25] and Papadiaz et al. [35]. For the sake of compactness, the reader is referred to these works for further details.

Jeifetz [36] compared the mass of active material required to attain the specification in CO exit composition for the case of effectiveness factors calculation and then assuming them as unity, for the range 423–463 K, obtaining a difference of a 2.5% in the worst of cases (at 463 K). Then, with the mass obtained for $\eta_{\text{H}_2} = \eta_{\text{CO}} = 1$, the CO exit composition was calculated, reaching a value of 22.55 ppm at 463 K, which is mild deviation from the original 19 ppm value for CO. With these results, we considered that it was safe to assume unitary effectiveness factors.

Re	Reynolds number	–
S	Global selectivity	–
Sc	Schmidt number	–
Sh	Sherwood number	–
T	Temperature	K
tcm	Total catalyst mass	kg
V_g	Catalyst pore volume	m ³ /kg
x	Conversion	–
y	Molar fraction	–
z	Reactor axial coordinate	m

Notation

a_{ch}	Channel cross section area open for the gas flow	m ²
b	Linear temperature profile slope	K/m
C_p	Heat specific capacity	J/mol.K
D	Molecular diffusivity	m ² /s
d_h	Channel hydraulic diameter	m
d_i	Monolith internal diameter	m
E_a	Activation energy	J/mol
F	Channel molar flow	mol/s
F_{total}	Monolith total molar flow	mol/s
g	Function defined in eq. (17)	–
Gr_m	Material Graetz number	–
Gr_t	Thermal Graetz number	–
h_{GS}	Heat transfer coefficient	W/m ² .K
k/K	Kinetic or adsorption constants	–
k^0/K^0	Pre-exponential constants	–
km	Mass transfer coefficient for molar fractions	mol/m ² .s
kmc	Mass transfer coefficient for concentrations	m/s
L	Monolith length	m
m	Cell side length	m
M	Molecular weight	g/mol
n_{ch}	Number of channels in the monoliths	–
Nu_{GS}	Nusselt number	–
P	Pressure	Pa
per_{ch}	Channel washcoat and gas phase contact perimeter	m
Pr	Prandtl number	–
r	Reaction rate	mol/g.s
R	Universal gas constant	J/mol.K
Rc	Radius in the channel corner	m

Greek letters

α	Support cross section fraction	–
β	Support thickness between consecutive channels	m
$\delta/2$	Washcoat thickness out of the channel corner	m
ΔH^{ads}	Adsorption enthalpy	J/mol
ΔH_r	Reaction enthalpy	J/mol
ΔT_{ad}^S	Temperature increase in an adiabatic monolith	K
ε	Gas phase cross section fraction	–
κ	Thermal conductivity	W/m.K
λ	Parameter defined in eq. (14)	–
μ	Viscosity	Pa.s
ξ	Washcoat cross section fraction	–
ρ	Density	kg/m ³

Subscripts and superscripts

ax	axial
e	Inlet condition
ef	Effective
f	Outlet condition
G	Relative to the gas phase
i, j	Species i, j
k	Monolith k in a series.
l	Kinetic or adsorption constant l
m	Reaction m
n	Iteration n
NR	Last monolith in a series
S	Relative to the solid phase
W	Relative to the catalytic solid
WP	Relative to the catalytic washcoat

References

- Giunta P, Amadeo N, Laborde M. Simulation of a low temperature water gas shift reactor using the heterogeneous model. Application to a PEM fuel cell. J Power Sources 2006;156:489–96.
- Ayastuy J, Gil-Rodríguez A, Gonzalez-Marcos M, Gutierrez-Ortiz M. Effect of process variables on Pt/CeO₂ catalyst behaviour for the PROX reaction. Int J Hyd Energy 2006;31:2231–42.
- Sirijaruphan A, Goodwin J, Rice R. Effect of temperature and pressure on the surface kinetic parameters of Pt/ γ -Al₂O₃ during selective CO oxidation. J Catal 2004;227:547–51.
- Lopez E, Kolios G, Eigenberger G. Preferential oxidation of CO in a folded-plate reactor. Chem Eng Sci 2007;62:5598–601.
- Echigo M, Shinke N, Takami S, Higashiguchi S, Hirai K, Tabata T. Development of residential PEFC cogeneration systems: Ru catalyst for CO preferential oxidation in reformed gas. Catal Today 2003;84:209–15.
- Moreno M, Baronetti G, Laborde M, Mariño F. Kinetics of preferential CO oxidation in H₂ excess (COPrOx) over CuO/CeO₂ catalysts. Int J Hyd Energy 2008;33:3538–42.

7. Sedmak G, Hocevar S, Levec J. Kinetics of selective CO oxidation in excess of H₂ over the nanostructured Cu_{0.1}Ce_{0.9}O_{2-y} catalyst. *J Catal* 2003;213:135–50.
8. Lee H, Kim D. Kinetics of CO and H₂ oxidation over CuO–CeO₂ catalyst in H₂ mixtures with CO₂ and H₂O. *Catal Today* 2008;132:109–16.
9. Giunta P, Moreno M, Mariño F, Amadeo N, Laborde M. COPrOx fixed bed reactor. Temperature control schemes. *Chem Eng Technol* 2012;35:1055–63.
10. Ávila P, Montes M, Miró E. Monolithic reactors for environmental applications. A review on preparation technologies. *Chem Eng J* 2005;109:11–36.
11. Cybulski A, Moulijn JA. The present and the future of structured catalysis – an overview. In: Cybulski A, Moulijn JA, editors. *Structured catalysts and reactors*. New York: Marcel Dekker, 1998:1–14.
12. Groppi G, Tronconi E. Honeycomb supports with high thermal conductivity for gas/solid chemical processes. *Catal Today* 2005;105:297–304.
13. Heck RM, Gulati S, Farrauto RJ. The application of monoliths for gas phase catalytic reactions. *Chem Eng J* 2001;82:149–56.
14. Tomašić V, Jović F. State-of-the-art in the monolithic catalysts/ reactors. *Appl Catal A Gen* 2006;311:112–21.
15. Korotkikh O, Farrauto R. Selective catalytic oxidation of CO in H₂: fuel cell applications. *Catal Today* 2000;62:249–54.
16. Gómez LE, Tiscornia IS, Boix AV, Miró EE. Co/ZrO₂ catalysts coated on cordierite monoliths for CO preferential oxidation. *Appl Catal A Gen* 2011;401:124–33.
17. Roberts GW, Chin P, Sun X, Spivey JJ. Preferential oxidation of carbon monoxide with Pt/Fe monolithic catalysts: interactions between external transport and the reverse water-gas-shift reaction. *Appl Catal B Environ* 2003;46:601–11.
18. Zhou S, Yuan Z, Wang S. Selective CO oxidation with real methanol reformat over monolithic Pt group catalysts: PEMFC applications. *Int J Hyd Energy* 2006;31:924–33.
19. Ahluwalia RK, Zhang Q, Chmielewski DJ, Lauze KC, Inbody MA. Performance of CO preferential oxidation reactor with noble-metal catalyst coated on ceramic monolith for on-board fuel processing applications. *Catal Today* 2005;99:271–83.
20. Zeng SH, Liu Y. Nd- or Zr-modified CuO–CeO₂/Al₂O₃/FeCrAl monolithic catalysts for preferential oxidation of carbon monoxide in hydrogen-rich gases. *Appl Surf Sci* 2008;254:4879–85.
21. Bissett EJ, Oh SH. PrOx reactor model for fuel cell feedstream processing. *Chem Eng Sci* 2005;60:4722–35.
22. Depcik C, Srinivasan A. One + One-dimensional modeling of monolithic catalytic converters. *Chem Eng Technol* 2011;34:1949–65.
23. Tronconi E, Groppi G, Boger T, Heibel A. Monolithic catalysts with “high conductivity” honeycomb supports for gas/solid exothermic reactions: characterization of the heat-transfer properties. *Chem Eng Sci* 2004;59:4941–9.
24. Arzamendi G, Uriz I, Diéguez PM, Laguna OH, Hernández WY, Álvarez A, et al. Selective CO removal over Au/CeFe and CeCu catalysts in microreactors studied through kinetic analysis and CFD simulations. *Chem Eng J* 2011;167:588–96.
25. Gonzo E. Hydrogen from methanol-steam reforming. Isothermal and adiabatic monolith reactors’ simulation. *Int J Hyd Energy* 2008;33:3511–16.
26. Groppi G, Tronconi E. Design of novel monolith catalyst supports for gas/solid reactions with heat exchange. *Chem Eng Sci* 2000;55:2161–71.
27. Chen J, Yang H, Wang N, Ring Z, Dabros T. Mathematical modelling of monolith catalysts and reactors for gas phase reactions. *Appl Catal A Gen* 2008;345:1–11.
28. Valentini M, Groppi G, Cristiani C, Levi M, Tronconi E, Forzatti P. The deposition of γ -Al₂O₃ layers on ceramic and metallic supports for the preparation of structured catalysts. *Catal Today* 2001;69:307–14.
29. Gracinsky C, Ubogui J, Sarto A, Tejada R, Laborde M, Francesconi J, et al. Hydrogen production from bioethanol: pilot plant scale. In: VI Chemical Engineering Argentinean Conference, Mar del Plata, Argentina, 2010.
30. Mariño F, Descorme C, Duprez D. Supported base metal catalysts for the preferential oxidation of carbon monoxide in the presence of excess hydrogen (PROX). *Appl Catal B Environ* 2005;58:175–83.
31. Moreno M. Hydrogen catalytic purification. PhD thesis, Engineering School, University of Buenos Aires, 2011.
32. Semeniuk HM. CuO/CeO₂/Al₂O₃ catalysts for the preferential oxidation of CO (COPrOx). Eng. thesis, Engineering School, University of Buenos Aires, 2011.
33. Elnashaie SS, Elshishini SS. Modelling, simulation and optimization of industrial fixed bed catalytic reactors. Amsterdam: Gordon and Breach Science Publishers, 1993.
34. Poulter C, Smith DS, Absi J. Thermal conductivity of pressed powder compacts: tin oxide and alumina. *J Eur Ceram Soc* 2007;27:475–8.
35. Papadakis D, Edsberg L, Björnbom P. Simplified method for effectiveness factor calculations in irregular geometries of washcoats. *Chem Eng Sci* 2000;55:1447–59.
36. Jeifetz LG. Monolithic reactors modelling for its application to the preferential CO oxidation reaction (COPrOx). Eng. thesis, Engineering School, University of Buenos Aires, 2012.